JOURNAL OF MATERIALS SCIENCE 19 (1984) 3855–3866

Metallurgical reaction and deposit fusion boundary microstructure under a stationary plasma arc

T. ISHIDA
The Research Institute for Iron, Steel and Other Metal, Tohoku University, Sendai, Japan

Alloy element loss, decarburization in melted region and microstructural change of a deposit fusion boundary under a stationary plasma arc have been investigated by a first-order kinetic and interfacial microstructure. The cylindrical specimens of iron-based alloys, Fe–C, Ni–C, and Co–C alloys were locally melted by a plasma arc using argon plasma gas and Ar + H_2 shielding gas, and the rates of alloy element loss and decarburization in the melted region were measured. Moreover, the fusion boundaries experienced when nickel, iron, Ni–Fe filler metals were deposited on iron, Fe–C, nickel and cobalt base metals, were evaluated metallographically. The initial rate of alloy element loss decreases as follows: Fe–Al > Fe–Mn > Fe–Cr > SGI–Mg > Fe–Ni. The loss reaction mechanism is metallic evaporation and the rate seems to be limited by transport in the gas boundary layer. The magnitude of decarburization is as follows: Ni–C > Fe–C > Co–C. The decarburization rate in Fe–C alloy is assumed to be governed by a process involving mass transfer in the gas phase and the molten metal. However, at low carbon concentrations, the rate appears to be limited by transfer in liquid metal. Fusion boundary deposited with nickel filler metal on iron is regular, but with carbon added to iron, an infiltration of deposit metal into adjacent base metal occurs. The fusion boundary with iron deposited on nickel is irregular where thin Ni–Fe solid solution is formed. In a deposited fusion boundary of cobalt with iron, nickel, and Ni–Fe filler metals, FeCo compound formation occurs, with cobalt dissolving into the nickel deposit metal resulting in a tongue-like structure produced by nickel penetration and a fine columnar substructure formation produced by Ni–Fe diffusion.

1. Introduction

Recently, there has been considerable interest in the production of intriguing microstructures and specific properties of local melting using an intense, collimated heat source, such as a laser or an electron beam [1–4]. However, a plasma arc having a high-powered energy is scarcely used for surface metal improvement of various materials. In this study, the metallurgical behaviour in the surface melted region, using the plasma arc producing a distinct contraction, has been investigated in connection with plasma arc welding.

Recent work by the author [5] has shown that fusion boundary microstructure of nodular cast iron by plasma arc local-melting with and without filler metal is characteristic of white iron, e.g. iron carbide plus eutectic, nickel-martensite and high carbon martensite. The report suggests that the variation of alloying element, e.g. carbon, silicon, magnesium, etc., exerts an effect on the fusion boundary microstructure and that the ionization phenomenon under the plasma arc is useful for the improvement of the structure of cast iron weld interface. Control of the composition and microstructure of the deposit weld metal is a prerequisite for weld metal with mechanical properties and corrosion resistance. A change of composition in the locally remelted region may

0022–2461/84 $03.00 + .12

occur under a plasma arc with a reducing atmosphere, where there is an ionized and a temperature-elevated plasma state. Moreover, the fusion boundary experienced when a filler metal is deposited on base metal under a plasma arc may be characteristic of a perfect interface microstructure as a sufficient weldment.

This knowledge of the significant factors and the interaction between the plasma arc stream and molten metal is lacking, and moreover, the microstructural aspect of the deposited fusion boundary by a plasma arc is insufficient. Most of the investigatory work associated with the problem of microstructural reaction of the weld interface by plasma arc with filler metal has been largely qualitative. Since both phases of the problem are important, two distinct experimental approaches have been adopted in this work.

The present research was carried out to measure rates of alloy element loss and decarburization in the melted region under a stationary plasma arc and to elucidate the reaction mechanism between the plasma arc and the molten metal, and further to determine microstructural change in the deposit fusion boundary between dissimilar metal, produced by a similar plasma arc local-melting method with filler metal. Specific attention is devoted to the metallurgical behaviour and the heterogeneous interface occurring under a plasma arc.

2. Experimental method

The base metals used in this experiment were Fe–Al, Fe–Mn, Fe–Cr, Fe–Ni and Fe–C–Si–Mg (spheroidal graphite cast iron, SGI) alloys for alloy element loss, Fe–C, Ni–C and Co–C alloys for decarburization and iron, Fe–C alloy, nickel and cobalt for filler metal depositing test. These base metals were prepared from 30 mm diameter mould castings with deoxidized and degassed vacuum melting of electrolytic iron, nickel, chromium, manganese and reagent aluminium, electrode carbon and Belgium-produced cobalt. For spheroidal graphite cast iron, the castings were produced by reduced [6] and magnesium-treated melting in an electric furnace, adding steel scrap to pig iron. The filler metals were provided from 10 mm diameter metal mould castings with deoxidized and degassed vacuum-melting of electrolytic nickel and iron.

Castings for the base metal were cut into specimen cylinders 30 mm in diameter and 25 mm in length. On the other hand, castings for the filler metal were forged and rolled into wire rod with a 4 mm diameter and 200 mm length. The filler metals employed were nickel, 50 wt % Ni–50 wt % Fe and iron.

The heat source for the local-melting procedure is a transferred plasma arc welder (Hitachi 300A). The base metal cylinder was melted locally under the stationary plasma torch at fixed time intervals. When the filler metal was used, it was inserted into the plasma arc and deposited onto the base metal. Plasma arc time, i.e. the occurrence time of the main arc, was from 10 to 40 sec. The welding current was 130 and 170 A, the plasma gas was argon with a flow rate of 2.8 $dm^3\ min^{-1}$, and the shielding gas was Ar + 10% H_2 and Ar + 20% H_2, with a flow rate of 13.0 $dm^3\ min^{-1}$. The electrode used was tungsten with a 6.0 mm diameter and a nozzle diameter of 3.0 mm. The distance from the nozzle to the base metal was 8 to 10 mm. The shielding gas was flowed in a given period of time after the disappearance of the arc.

After the local arc-melting procedure, the chemical analyses in the melted region were made, whereas the specimens deposited by filler metal were partly analysed chemically to obtain the chemical composition of the deposit metal, and cross-sectioned, polished and then etched in 5% nital and mixed acid etchants for optical microscope observation.

3. Results and discussion

3.1. Alloy element loss

Fig. 1 shows the results of alloy element loss from the melted region as a function of the plasma arc-time. Of the common alloy elements in iron alloys, nickel loss does not occur under the plasma arc, but aluminium, chromium, manganese and magnesium losses take place. The degree of loss of alloying element is large in the initial stage of the reaction and gradually falls off with the lapse of time. This phenomenon is seen to be a part of solute atoms evaporated in the argon stream probably returning again to the melt surface.

Loss behaviour of the solute atom indicates a first-order reaction which may be described by:

$$-\frac{dc}{dt} = k\frac{A}{V}C = KC \qquad (1)$$

which integrates to give [7]:

$$2.303 \log \frac{C_0}{C} = k\frac{A}{V}t = Kt \qquad (2)$$

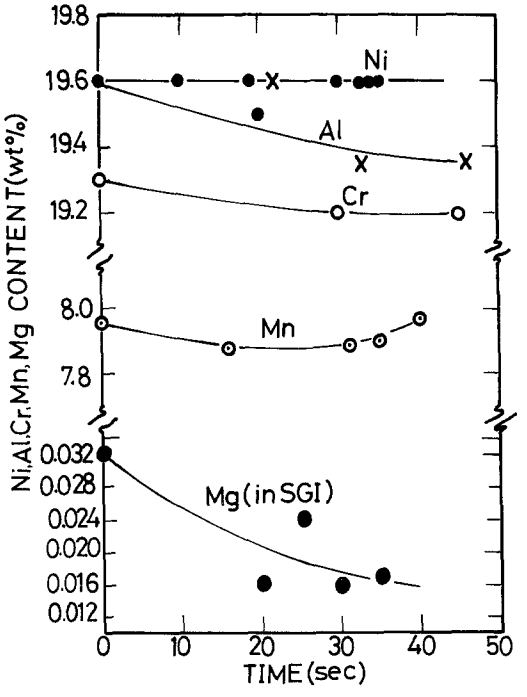

Figure 1 Loss of alloy elements from the plasma arc melted region for iron-based alloys and spheroidal graphite cast iron using argon plasma gas and Ar + 10% H_2 shielding gas at arc current 130 A.

where C is the bulk solute concentration (wt%), C_0 is the initial solute concentration (wt%), k(cm sec^{-1}) and K(sec^{-1}) are first-order rate constants, A is the interface area (cm^2), and V is the melt volume (cm^3). The logarithm of the melt composition was plotted against time in Fig. 2

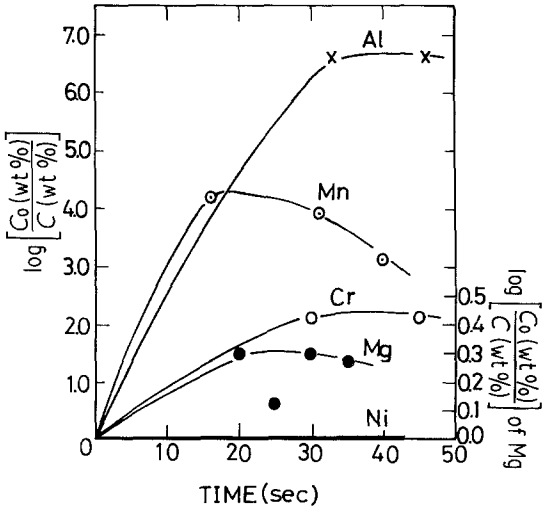

Figure 2 First order plots of alloy element loss from the plasma arc melted region for iron-based alloys and spheroidal graphite cast iron.

TABLE I The values of melt composition, initial loss-rate and rate constant for alloy elements in the melted region under a stationary plasma arc using argon plasma gas and Ar + 10% H_2 shielding gas at an arc current of 130 A

Alloy	t(sec)	C(wt%)	v_0(wt% sec^{-1})	K_0(sec^{-1})
Fe–Al	0	19.6		
	22	19.6	7.0×10^{-3}	4.68×10^{-4}
	33	19.3		
	46	19.3		
Fe–Cr	0	19.3		
	30	19.2	3.33×10^{-3}	1.74×10^{-4}
	45	19.2		
Fe–Mn	0	7.96		
	16	7.88		
	31	7.89	5.0×10^{-3}	6.32×10^{-4}
	35	7.90		
	40	7.97		
Fe–Ni	0	19.6		
	10	19.6		
	19	19.6		
	20	19.5	0	–
	30	19.6		
	33	19.6		
	35	19.6		
SGI–Mg	0	0.032		
	20	0.016		
	25	0.024	5.45×10^{-4}	3.47×10^{-2}
	30	0.016		
	35	0.017		

for the iron alloys. The nonlinear relationship between $\log C_0/C$ and t of Equation 2 was obtained for all the elements. This accounts for the returning effect of a part of evaporated solute atoms onto the melt surface with the elapse of time. In vacuum, evaporating atoms are regarded not to return onto the melt surface. On the other hand, in the argon stream, solute atoms evaporated once collide and repulse each other with argon atoms or other solute atoms and they take occasion to return again onto the melt surface [8]. Therefore, for all the time range of this experiment this first-order equation cannot be fitted. The magnitude of this returning effect is as follows: Mn > Mg > Al > Cr > Ni. Since then, attention was paid to the treatment of the early reaction of alloy element loss, where the returning effect can be ignored. The values of the initial rate, v_0, and the initial rate constant, K_0, obtained in this experiment for alloy element loss are given in Table I. The initial rate decreases in the following sequence:

Fe–Al > Fe–Mn > Fe–Cr > SGI–Mg > Fe–Ni

The reaction mechanism responsible for the loss

of alloy elements from the melted region under the plasma arc is poorly understood, but one can envisage two major types of mechanism: metallic evaporation and reactions with other elements such as, in the plasma state, H ion or molecule in the shielding gas to form gases or solid compounds. The results of initial reactions obtained in this experiment are that the loss behaviour is similar to that of vacuum induction melting [7, 9, 10] for iron alloy. Ward [9] reported that evaporation loss of manganese from induction melted steel was large and the rate of loss was limited by both transport in the metal boundary layer and evaporation from the metal surface. The rate decreases with increase in pressure of argon and at 1 atm pressure the rate is predominantly limited by transport in the gas boundary layer. The initial loss-rate constant, k_0 obtained in this experiment is very close to the evaporation rate-constant of k_{Mn} measured in argon at high pressure. As a result, it may be surmized that the alloy element is lost by an evaporation mechanism without reaction with other elements and that the mass transfer in the gas phase is rate controlling.

3.2. The decarburization of Fe–C, Ni–C and Co–C alloys

It became evident that decarburization occurred under the plasma arc. This behaviour is of great importance in plasma arc welding for iron-based materials.

The decarburization rate, v (wt% sec^{-1}) also, may be expressed by the same first-order reaction for the alloy element loss,

$$v = -\frac{dn}{dt} = k_c \frac{A}{V} n = K_c n \qquad (3)$$

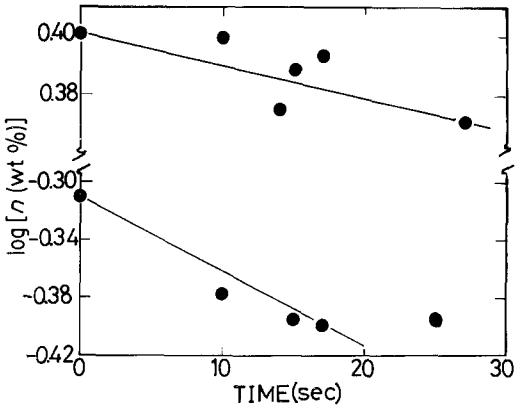

Figure 3 Logarithmic plots of carbon concentration against arc time for Fe–C alloys at an arc current of 130 A using argon plasma gas and Ar + 10% H_2 shielding gas.

which integrates to give:

$$\ln \frac{n_0}{n} = k_c \frac{A}{V} t = K_c t \qquad (4)$$

where n and n_0 are the bulk carbon concentration (wt%) and the initial bulk carbon concentration (wt%), respectively, k_c(cm sec^{-1}) and K_c(sec^{-1}) are decarburization rate constants.

Fig. 3 shows the plots of logarithm of carbon concentration against the plasma arc-time in Fe–C alloy melted region by plasma arc local-melting with an arc current of 130 A, using argon plasma gas and Ar + 10% H_2 shielding gas. The chemical analyses of the melted region with the arc time, the rate of decarburization, v, and the rate constant, K_c, are given in Table II. The rate of decarburization is higher at high carbon concentration than at low carbon concentration. Furthermore, Fig. 4 shows the change in carbon content as a function of time in the Fe–C alloy-

TABLE II The values of melt composition, decarburization rate and rate constant in plasma arc locally melted region of Fe–C alloys at an arc current of 130 A using argon plasma gas and Ar + 10% H_2 shielding gas

Alloy	t(sec)	n(wt%)	v(wt% sec^{-1})	K_c(sec^{-1})
Fe–0.49% C	0	0.49		
	10	0.42		
	15	0.41	5.0×10^{-3}	1.19×10^{-2}
	17	0.40		
	25	0.41		
Fe–2.52% C	0	2.52		
	10	2.51		
	14	2.37	7.0×10^{-3}	2.59×10^{-3}
	15	2.45		
	17	2.48		
	27	2.35		

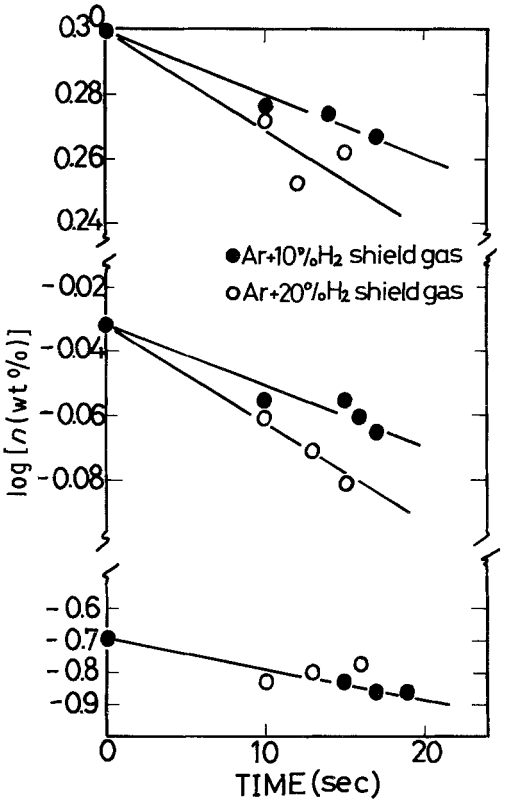

Figure 4 Logarithmic plots of carbon concentration against arc time for Fe–C alloys at an arc current of 170 A using argon plasma gas and Ar + 10% H_2 and Ar + 20% H_2 shielding gases.

melted region at an arc current of 170 A, using argon plasma gas and Ar + 10% H_2 and Ar + 20% H_2 shielding gases. These experimental results are listed in Table III. The rate of decarburization is high with a high carbon content and increases with increase in hydrogen in the shielding gas; however, at low carbon concentration the rate is not influenced by hydrogen increase in the shielding gas.

The decarburization also occurred in Ni–C and Co–C alloys. These results are given in Figs. 5 and 6 and the various values obtained in this experiment are presented in Table IV. The rate of decarburization of Ni–C alloy decreases with the increase in carbon concentration, while that of Co–C alloy increases with the increase in carbon concentration. Fig. 7 shows the dependence of carbon concentration on the rate of decarburization in Fe–C, Ni–C and Co–C alloys. The rate decreases as follows:

$$\text{Ni–C} > \text{Fe–C} > \text{Co–C}$$

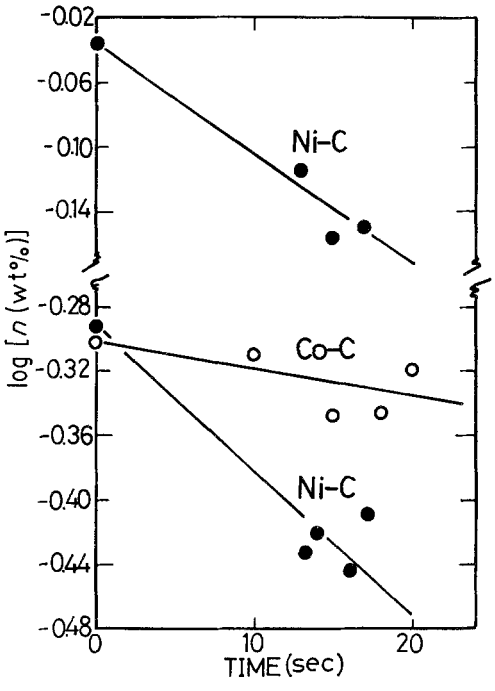

Figure 5 Logarithmic plots of carbon concentration against arc time for Ni–C and Co–C alloys with low carbon concentration at an arc current of 170 A using argon plasma gas and Ar + 10% H_2 shielding gas.

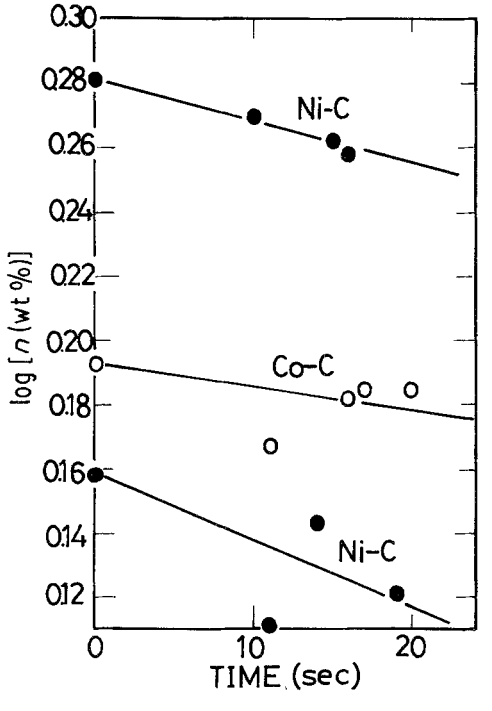

Figure 6 Logarithmic plots of carbon concentration against arc time for Ni–C and Co–C alloys with high carbon concentration at an arc current of 170 A using argon plasma gas and Ar + 10% H_2 shielding gas.

TABLE III Effect of hydrogen in the shielding gas on the decarburization in plasma arc locally melted region of Fe–C alloy at an arc current of 170 A

Alloy	t (sec)	n (wt %)	v (wt % sec^{-1})	K_c (sec^{-1})
(a) Shielding gas Ar + 10% H_2				
Fe–0.20% C	0	0.20		
	10	0.15		
	15	0.15	3.81×10^{-3}	2.11×10^{-2}
	17	0.14		
	19	0.14		
Fe–0.93% C	0	0.93		
	10	0.88		
	15	0.88	4.12×10^{-3}	4.36×10^{-3}
	16	0.87		
	17	0.86		
Fe–1.99% C	0	1.99		
	10	1.89	8.24×10^{-3}	4.34×10^{-3}
	14	1.88		
	17	1.85		
(b) Shielding gas Ar + 20% H_2				
Fe–0.20% C	0	0.20		
	10	0.15	3.81×10^{-3}	2.11×10^{-2}
	13	0.16		
	16	0.17		
Fe–0.93% C	0	0.93		
	10	0.87	6.67×10^{-3}	7.10×10^{-3}
	13	0.85		
	15	0.83		
Fe–1.99% C	0	1.99		
	10	1.87	12.7×10^{-3}	6.91×10^{-3}
	12	1.79		
	15	1.83		

The rate of decarburization is dependent on carbon concentration.

As can be seen from Fig. 4 and Table III, the rate of decarburization in Fe–C alloys is strongly hydrogen-atmosphere dependent. An increase of the decarburization rate in molten iron due to the increase of hydrogen in the shielding gas indicates that hydrogen contributes greatly to the decarburizing effect in the iron melt. Schematic representation of the reaction occurring between the plasma arc and the molten metal is illustrated in Fig. 8.

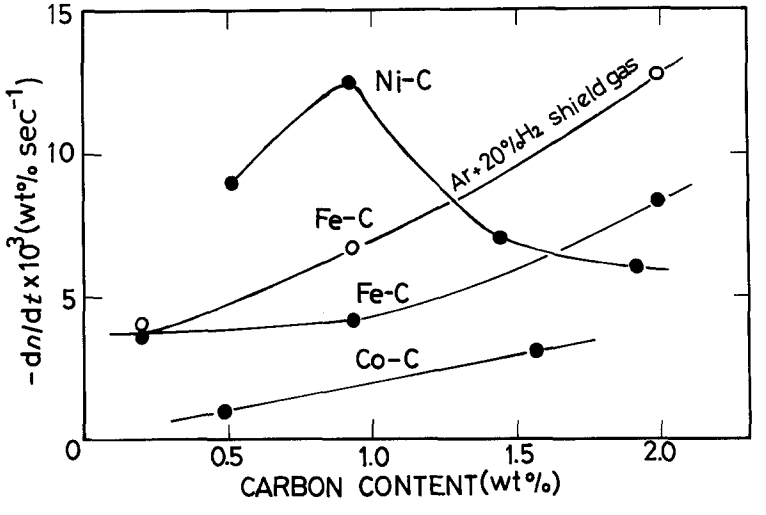

Figure 7 Effect of carbon concentration on the decarburization rate in Fe–C, Ni–C and Co–C alloys at an arc current of 170 A using argon plasma gas and Ar + 10% H_2 shielding gas.

TABLE IV The values of melt composition, rate and rate constant for the decarburization in plasma arc locally melted region of Ni–C and Co–C alloys at an arc current of 170 A using argon plasma gas and Ar + 10% H_2 shielding gas

Alloy	t (sec)	n (wt %)	v (wt % sec^{-1})	K_c (sec^{-1})
Ni–0.51% C	0	0.51		
	13	0.37		
	14	0.38	9.0×10^{-3}	2.07×10^{-2}
	16	0.36		
	17	0.39		
Ni–0.92% C	0	0.92		
	13	0.77	12.5×10^{-3}	1.53×10^{-2}
	15	0.70		
	17	0.71		
Ni–1.44% C	0	1.44		
	11	1.29	7.0×10^{-3}	4.75×10^{-3}
	14	1.39		
	19	1.32		
Ni–1.91% C	0	1.91		
	10	1.86	6.0×10^{-3}	2.92×10^{-3}
	15	1.83		
	16	1.81		
Co–0.50% C	0	0.50		
	10	0.49		
	15	0.45	1.0×10^{-3}	1.73×10^{-3}
	18	0.45		
	20	0.48		
Co–0.50% C	0	1.56		
	11	1.47		
	16	1.52	3.0×10^{-3}	3.98×10^{-3}
	17	1.53		
	20	1.53		

When argon gas reaches the plasma state, the plasma column temperature is above 10 000 K [11] and hydrogen molecules in the shielding gas are dissociated into hydrogen atoms, where hydrogen exists in atomic and ionic states. However, when the plasma gas is blown on the metal surface with a relative lowering of the temperature, hydrogen ions having a positive charge are considered to be unable to reach at an ionic state to the metal surface, because the temperature of the gas phase at the metal surface decreases and H^+ causes an electrical repulsion, through the metal side acting as an anode. If hydrogen participates in the decarburization when it is atomic hydrogen, the gas species may produce reaction products such as CH, CH_2, CH_4, C_2H_2, etc. These reactions are indicated in Fig. 8. Kaneko *et al.* [12] have reported that atomic hydrogen, dissociated in the plasma jet where the $2H \rightarrow H_2$ reaction may be produced in the "frozen-in" state, reacts directly with the carbon in the molten iron and that the main product species is most possibly CH_4. In this experiment, too, as the collision frequency is very low under low partial pressure of hydrogen, the reassociation of dissociated hydrogen gas does not occur. Therefore, it is considered to be atomic state hydrogen being allowed to react with the carbon in the molten iron.

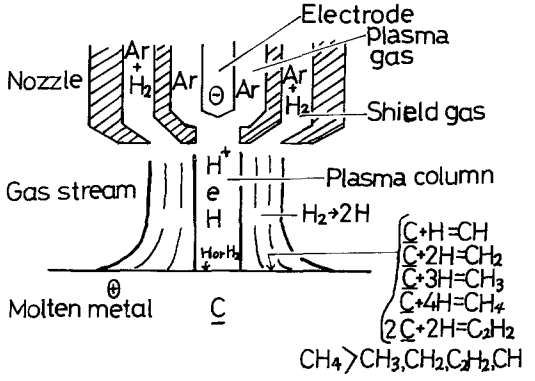

Figure 8 Schematic representation showing decarburization reaction occurring between plasma arc and molten metal.

The decarburization reaction is conveniently roughly divided into the following phenomena:

(i) Mass transfer in the gas phase,
(ii) Interfacial chemical reaction,
(iii) Mass transfer in the liquid phase.

The observed rate may be dominated or influenced by one or more of these steps. Of these steps, the chemical reaction step can be very fast at this high temperature. Therefore, this step has not been taken into consideration in the results. The rate of decarburization in Fe–C and Co–C alloys is proportional to the carbon concentration and in Ni–C alloy to the reciprocal of the concentration. From these concentration dependencies, it suggests that the mass transfer in the liquid metal phase is rate controlling. On the other hand, the rate in Fe–C alloy is also dependent on the partial pressure of hydrogen. This fact cannot ignore the effect of mass transfer in the gas phase. As a result, this observation lends support to the view that at high carbon concentration the mass transfer in the gas phase and liquid metal is a rate-controlling step at least, and at low carbon concentration the rate-determining step is the mass transfer of metal liquid phase.

3.3. Microstructures of deposit metal and fusion boundary

Melting and depositing rates of filler metal in a more constricted region of the plasma arc are very high. The cross-section of the deposit in the form of beads on the base metal is not a wine-glass configuration, but an overlay shape (Fig. 9). The width of the deposit metal, W, expresses a diameter of bead and depth of penetration, D, is rather small. The test results are summarized in Table V. The shape of the fusion boundary appears to be dependent on the difference of melting point of filler metal. When filler metal, having a high melting point, is used, the disturbed fusion boundary region due to the vigorous reaction between dissimilar metal is recognised.

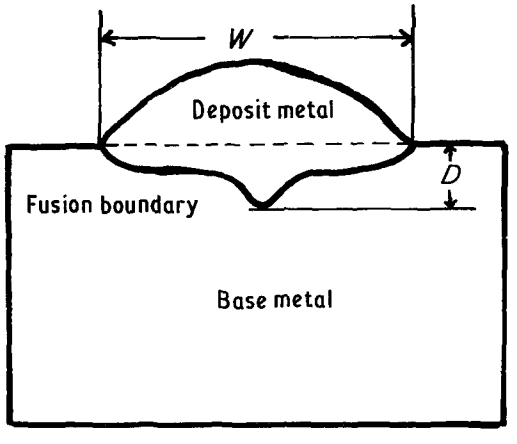

Figure 9 Cross-section of the deposit metal in the form of a bead by stationary plasma arc local-melting with filler metal.

3.3.1. Nickel or Ni–Fe deposited on iron and Fe–C alloy

Fig. 10 shows the microstructures of deposited fusion boundary regions of iron and Fe–0.49 wt% C base metals with nickel or Ni–50 wt% Fe filler metal. In the case of nickel deposited on iron, the deposit metal is an austenitic structure with the Ni–Fe alloy and the fusion line is rather regular, as shown in Figs. 10a and b. In the case of nickel deposited on Fe–C, the fusion boundary region is irregular and the infiltration of filler metal into the adjacent base metal occurs, as can be seen in Figs. 10c and d, indicating a layer of nickel migration into the heat affected zone. This infiltration process is diffusion controlled and treated with grain boundary wetting concepts of a liquid–solid interface [13]. In the case of Ni–Fe alloy deposited on Fe–C alloy, a large amount of Ni–Fe martensite precipitated in the deposit metal (Fig. 10e) and at the deposit metal side of the fusion boundary region small nodular graphites in the Ni–Fe alloy matrix was observed. The fusion line is somewhat irregular and the nickel migration layer into the adjacent base metal was observed in the fusion boundary, as seen in Fig. 10f.

3.3.2. Iron deposited on nickel

Fig. 11 shows the microstructures of the deposit metal and the fusion boundary region of nickel deposited with iron filler metal. The deposit metal had a fully developed cellular structure (Fig. 11a) and the fusion line was irregular (Fig. 11b). In the fusion boundary region a very thin Ni–Fe solid solution layer (considered to be $FeNi_3$) could be formed.

3.3.3. Iron, nickel and Ni–Fe alloy deposited on cobalt

Fig. 12 shows the microstructures of the deposited fusion boundary region of cobalt with iron, nickel and Ni–50 wt% Fe filler metals. In the case of iron deposited on cobalt, FeCo metal formation occurs in the deposit metal and fusion boundary region (Fig. 12a). It can be seen from Fig. 12b

TABLE V Observed data of deposit metal composition, bead geometry and microstructural features obtained when nickel, iron and Ni–Fe filler metals are deposited on iron, Fe–C, nickel and cobalt base metals

Base metal	Filler metal (Melting point ° C)	Composition of deposit metal (wt%)	Width of deposit metal, W (mm)	Depth of penetration, D (mm)	Microstructural feature of discrete regions in deposited fusion boundary	
					Deposit metal	Fusion boundary region
Fe	Ni (1455)	–	23.9	3.90	Ni austenitic matrix	Flat interface
Fe–0.49 wt% C	Ni (1455)	–	24.3	4.0	Ni–Fe–C matrix	Infiltration of deposit metal into the adjacent base metal
Fe–0.49 wt% C	50 wt% Ni–50 wt% Fe (1438)	–	25.4	3.1	Ni–Fe martensites, small nodular graphites	Slightly irregular interface
Ni	Fe (1536)	Ni: 23.2	20.5	2.10	Fully developed cellular substructure	Irregular interface
Co	Fe (1536)	Co: 47.3	19.8	3.35	FeCo precipitated in matrix	Thin FeCo layer formation
Co	Ni (1455)	Co: 29.4	20.9	2.8	Ni–Co alloy	Tongue-like structure by penetration of Ni into adjacent base metal
Co	50 wt% Ni–50 wt% Fe (1438)	Co: 44.2 Ni: 26.0 Fe: 29.8	24.3	2.5	Ni–Fe–Co alloy	Fine columnar substructure by diffusion of deposited Ni–Fe into adjacent base metal

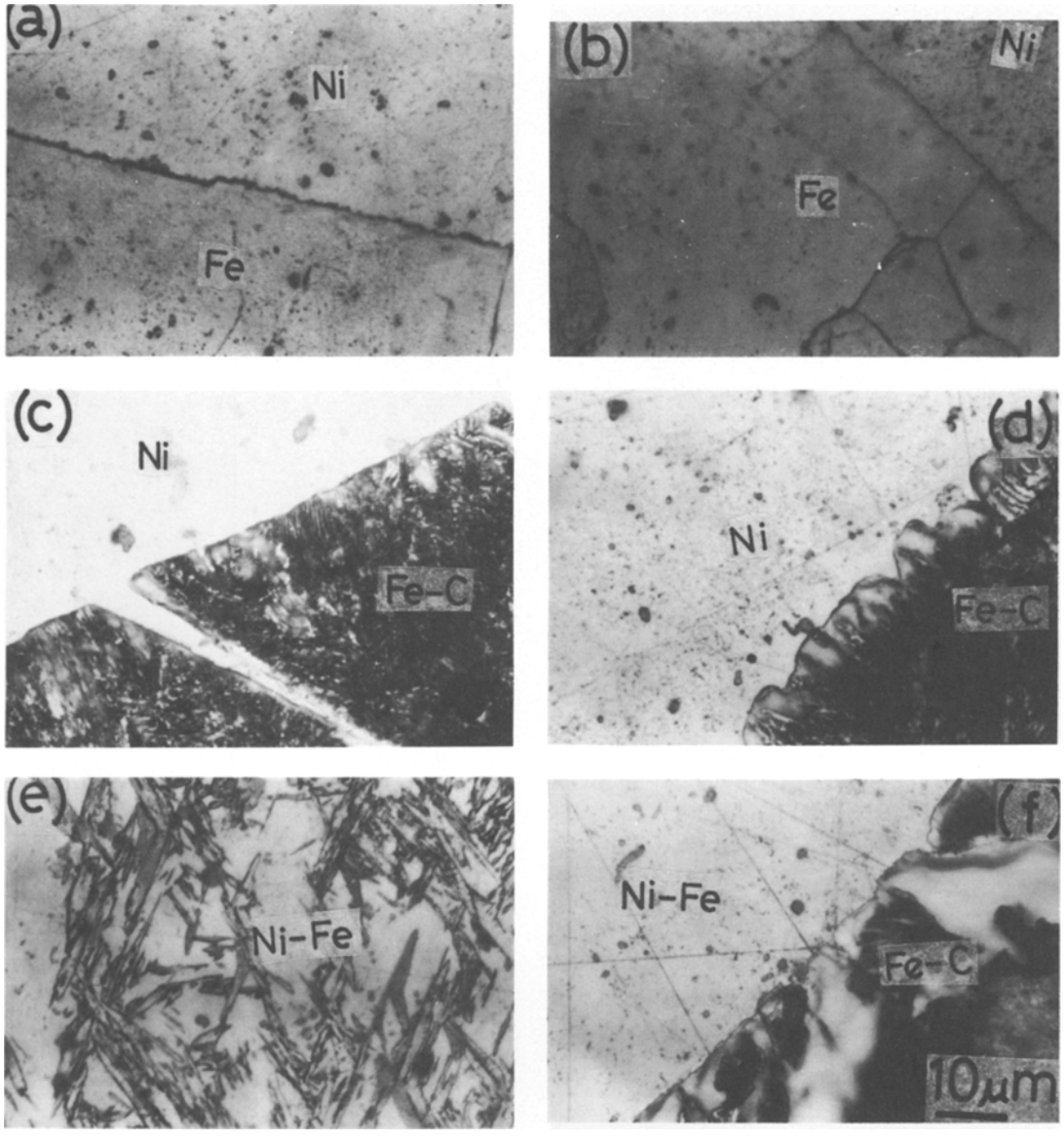

Figure 10 Microstructures of the fusion boundary obtained when nickel and Ni–Fe filler metals are deposited on iron, Fe–C base metals using argon plasma gas and Ar + 10% H_2 shielding gas at an arc current of 130 A. (a) and (b) Nickel deposited on iron, (c) and (d) nickel deposited on Fe–0.49% C, (e) and (f) Ni–50% Fe deposited on Fe–0.49% C. Mixed acid etched.

that a great amount of cobalt base metal dissolving into the deposit-metal side occurs in the fusion boundary region. In the case of nickel deposited on cobalt, in the deposit metal a Ni–Co solid solution is formed and in the fusion boundary region a tongue-like structure is observed in the heat affected zone immediately adjacent to the fusion line, as shown in Figs. 12c and d. This tongue-like structure seems to form as a result of alloy growth by nickel filler metal penetration into the cobalt base metal. In the case of Ni–Fe deposited on cobalt, the deposit metal has a matrix of Ni–Fe–Co alloy and the fusion boundary region consists of Ni–Fe–Co alloy at the deposit-metal side and a finely columnar substructure at the adjacent base metal (Figs. 12e and f). This finely columnar substructure indicates that the molten filler metal Ni–Fe alloy has penetrated or substitutionally diffused deeply into the adjacent base metal cobalt.

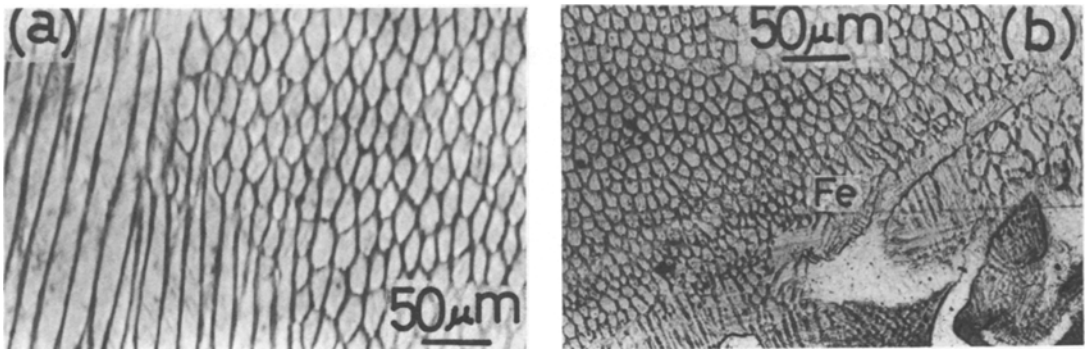

Figure 11 Microstructures of (a) deposit metal and (b) fusion boundary, obtained when iron filler metal is deposited on nickel base metal using argon plasma gas and Ar + 10% H_2 shielding gas at an arc current at 130 A. Nital etched.

4. Conclusions

Alloy element loss and decarburization from the melted region and microstructural change of deposit fusion boundary under a stationary plasma arc have been investigated by a first-order reaction and metallography, and the following results were obtained.

1. The loss of alloy element under a plasma arc is relatively small and the initial loss rate decreases as follows: Fe–Al > Fe–Mn > Fe–Cr > SGI–Mg > Fe–Ni. In the loss process, a part of the solute atoms evaporating in the argon stream seems to take occasion to return again to the melt surface with the lapse of time.

2. The alloy element is lost by an evaporation mechanism without reaction with other elements

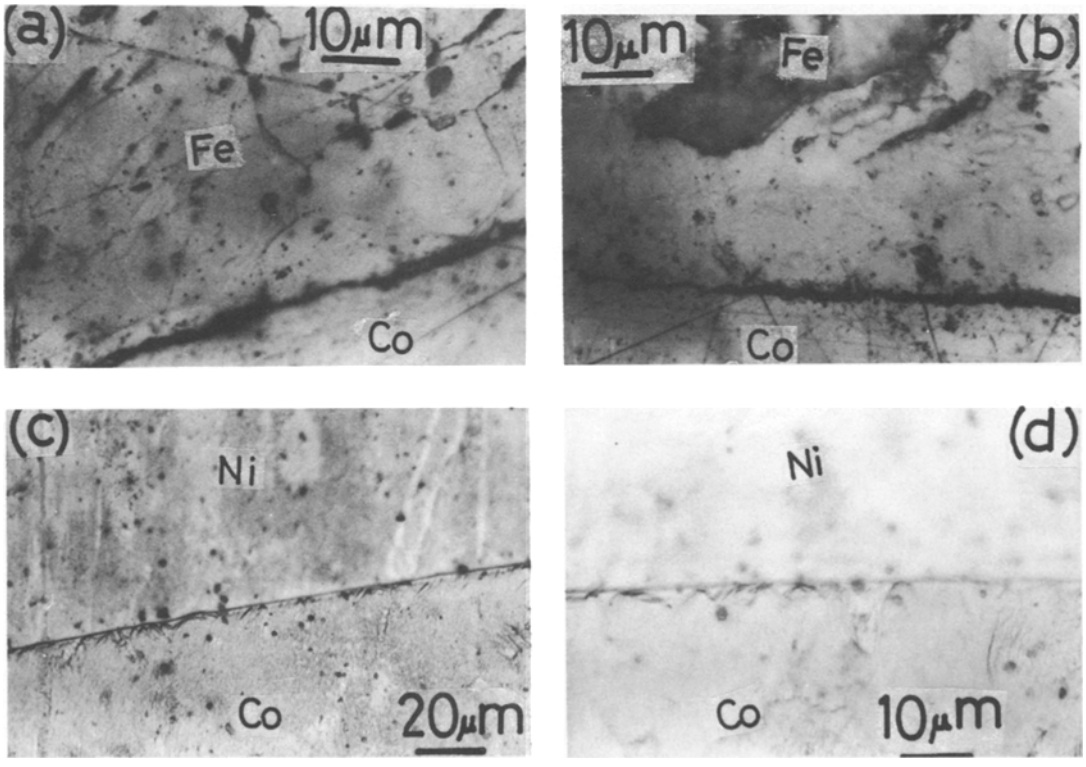

Figure 12 Microstructures of the fusion boundary obtained when iron, nickel and Ni–Fe filler metals are deposited on cobalt base metal using argon plasma gas and Ar + 10% H_2 shielding gas at an arc current of 130 A. (a) and (b) Iron deposited on cobalt, (c) and (d) nickel deposited on cobalt, and (e) and (f) Ni–50% Fe deposited on cobalt. Mixed acid etched.

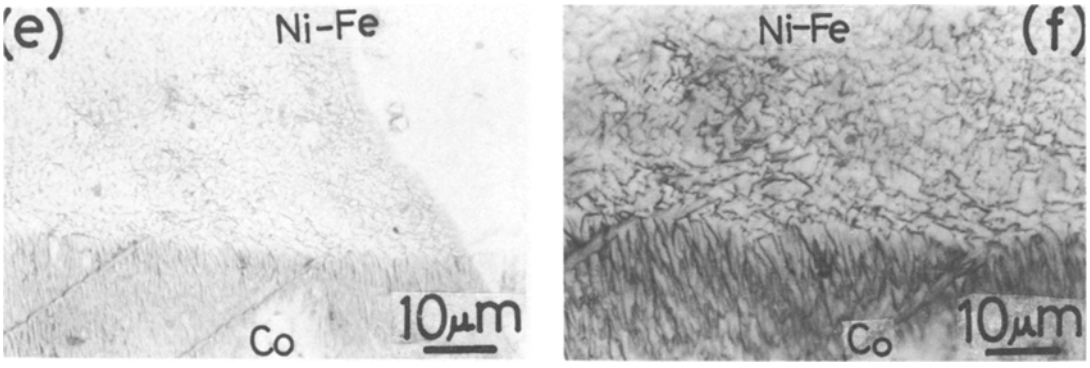

Figure 12 Continued.

and the loss rate appears to be limited by the mass transfer in the gas phase.

3. The rate of decarburization in Fe–C alloy is high with high carbon concentrations and increases with increase in hydrogen in the shielding gas. However, at low carbon concentrations the rate is not influenced by the increase in hydrogen in the shielding gas. The rate of decarburization decreases as follows: Ni–C > Fe–C > Co–C.

4. The decarburization mechanism is that atomic state hydrogen in the plasma arc column is allowed to react with the carbon in the molten metal. The decarburization rate seems to be mixed-controlled by both mass transfer in gas and liquid metal at high carbon concentration, and at low carbon concentration the rate is controlled by mass transfer in the liquid metal.

5. Fusion boundary nickel deposited on iron is regular, but nickel and Ni–Fe deposited on Fe–C is irregular where an infiltration of deposit metal into adjacent base metal occurs.

6. Fusion boundary iron deposited on nickel is irregular where thin Ni–Fe solid solution is formed at the interface. In the fusion boundary iron, nickel and Ni–Fe deposited on cobalt, FeCo compound formation, cobalt dissolving into the nickel deposit metal, the tongue-like structure produced by nickel penetration into the cobalt base metal and fine columnar substructure of the adjacent cobalt base metal, produced by diffusion of deposit Ni–Fe metal into adjacent cobalt base metal, are observed.

Acknowledgements

The author would like to thank Mr S. Yamada and Mr K. Enami for the specimen preparation, and Dr S. Takeyama, Mr M. Hosoya, Mr M. Takeuchi, Mr K. Tozawa and Mr H. Danzaki for the chemical analyses of the alloy elements.

References

1. T. CHANDE and J. MAZUMDER, *Metall. Trans.* **14B** (1983) 181.
2. G. CHRISTODOULOU, A. WALKER, W. M. STEEN and D. R. F. WEST, *Met. Technol.* **10** (1983) 215.
3. H. W. BERGMANN and B. L. MORDIKE, *J. Mater. Sci.* **16** (1981) 863.
4. B. G. LEWIS and P. R. STRUTT, *JOM* **34** (1982) 37.
5. T. ISHIDA, *J. Mater. Sci.* **18** (1983) 1773.
6. M. HOMMA and T. ISHIDA, *Sci. Rep. RITU* **A-17** (1965) 1.
7. R. G. WARD, *J. Iron Steel Inst.* **201** (1963) 11.
8. K. ITO and K. SANO, *Tetsu-to-Hagané* **50** (1964) 1161.
9. R. G. WARD and T. D. AURINI, *J. Iron Steel Inst.* **104** (1966) 920.
10. R. OHNO and T. ISHIDA, *ibid.* **206** (1968) 904.
11. D. A. GERDEMAN and N. L. HECHT, "Arc Plasma Technology in Materials Science" (Springer-Verlag, New York, 1972) p. 4.
12. K. KANEKO, N. SANO and Y. MATSUSHITA, *Trans. ISIJ* **16** (1976) 680.
13. S. J. MATTHEWS and W. F. SAVAGE, *Weld. J.* **50** (1971) 174s.

Received 23 September
and accepted 14 December 1983